A Note on the Use of Dynamic Mode Decomposition in Mechanics

C. Hari Manoj Simha and Mohammad Biglarbegian

School of Engineering, University of Guelph, 50 Stone Road East, Guelph, ON, Canada N1G 2W1

Abstract

We advocate for the use of Dynamic Mode Decomposition (DMD) in mechanics. Snapshots of the temperature or displacement fields are obtained; and the DMD algorithm, which, remarkably, requires a few lines of code, is applied to matrices obtained by time shifting the snapshots. Only the higher-order modes are retained to obtain a lower-rank matrix and used for analysis. We show that DMD can be used to: predict temperature fields during transient heat conduction, estimate natural frequency of a linear elastic structure; identify the onset of plasticity in an elastic-plastic plate with a hole; and obtain a reduced-order model that describes the large deformation of a non-linear elastic structure.

Keywords: Data-driven; Dynamic Mode Decomposition; Solid Mechanics; Reduced-Order Model

1. Introduction

Eulerian measurements or results from Computational Fluid Dynamics (CFD) computations of velocity, temperature, and pressure in flow fields, can be post-processed using a popular data-driven algorithm called Dynamic Mode Decomposition (DMD). Developed by Schmid [10] and Rowley et al. [7], and applied to flow in channels and jets by Rowley et al. [7] and Schmid et al. [9], and it is noteworthy that within a decade of its introduction it has been applied in thermo-fluids, neuroscience, image processing, and epidemiological studies; Brunton and Kutz [3]. The most recent version of the algorithm, theoretical background, limitations of the method, its connection with the Koopman operator, open questions, and associated bibliography may be found in the monograph by Kutz et al. [6] and text by Brunton and Kutz [3].

At its essence, it takes as input a sequence of temporal snapshots of field variables (velocity temperature, displacement measurements), and sets up a data matrix by time shifting the snapshots. The resultant data matrix may be excessively large, especially in CFD computations. However, the DMD algorithm carries out a Singular Value Decomposition (SVD), which allows selection and retention of only the dominant modes in the system. Retaining only the dominant modes, leads to a lower-rank matrix, *which is significantly smaller than the larger data matrix and whose eigenvalues and eigenvectors describe the dynamics of the system.* For linear systems, the DMD algorithm obtains the leading eigenvalues and eigenvectors; and for periodic data, the decomposition is equivalent to a discrete Fourier transform; Rowley et al. [7].

Despite its popularity, DMD has not been applied by the solid mechanics community save two instances. Saito and Kuno [8] applied it to measurements on a vibrating cantilever and obtained its natural frequency and damping coefficient. Das et al. [4] used DMD as well as Proper Orthogonal Decomposition (POD), with states obtained from finite element computation, to model the deformed state of a pneumatic finger; they, however, used displacements and velocities in their representation of states. In solid mechanics, with the prevalence of Digital Image Correlation (DIC) systems, snapshots of displacements are readily obtained, but not velocities.

This letter demonstrates the use of a data-driven approach in typical mechanics problems: transient heat conduction; vibration of a circular plate; identifying onset of plasticity in a elastic-plastic structure; and reduced-order model for a non-linear elastic structure undergoing large deformation. Systems in the first two instances are linear. Nonlinearity in the third is owing to the material response, and in the last because of the material response *and* large deformation.

2. Background on DMD

Notation and treatment in this section is similar to that in Brunton and Kutz [3]. Assume that the data (computational or experimental) is collected from a dynamical system $d\boldsymbol{x}/dt = \boldsymbol{f}(\boldsymbol{x}, t; \mu)$; where $\boldsymbol{x}$ is a state vector at time t, $\boldsymbol{f}$ denotes the dynamics, and μ represents parameters of the system. The DMD approach assumes local linearity of the above and takes

$$\frac{d\boldsymbol{x}}{dt} = \mathcal{A}\boldsymbol{x} \; ; \tag{1}$$

which has the solution $\boldsymbol{x}(t) = \exp(\boldsymbol{\mathcal{A}}t)\boldsymbol{x}(0)$, where $\boldsymbol{x}(0)$ is the initial condition. The modal matrix of $\mathcal{A}$ comprising its eigenvectors is $\boldsymbol{M} = [\xi_1, \;\; \xi_2 \;\; ... \; \xi_n]$, and it is a standard result that $\boldsymbol{x}(t) = \boldsymbol{M}\exp(\boldsymbol{\Omega}t)\boldsymbol{M}^{-1}\boldsymbol{x}(0)$, where $\boldsymbol{\Omega}$ is the diagonal matrix containing eigenvalues of $\mathcal{A}$; see section 10 of Brogan [2], for instance.

The DMD approach solves Eq. (1) by obtaining snapshots $\boldsymbol{x}$ of the system $\boldsymbol{f}(\cdot)$. Assuming that there are $m+1$ snapshots (vectors) each containing n measurement that describe the state of the system, time-shift them and insert as columns in $\boldsymbol{X}$ of size $n \times m$ and $\boldsymbol{X}'$ of size $n \times m$ to get

$$\boldsymbol{X} = [\boldsymbol{x}_1 \;\; \boldsymbol{x}_2 \cdots \; \boldsymbol{x}_m] \text{ and} \tag{2}$$

$$\boldsymbol{X}' = [\boldsymbol{x}_2 \;\; \boldsymbol{x}_3 \cdots \; \boldsymbol{x}_{m+1}] \; . \tag{3}$$

Later we show a modified strategy for assembling $\boldsymbol{X}$ for systems with standing waves; see Tu et al. [12] in this regard. Here, we assume that the snapshots are sampled at constant intervals Δt. The essence of DMD is determination of a best-fit operator $\boldsymbol{A}$ that advances the initial state to the next as

$$\boldsymbol{X}' = \boldsymbol{A}\boldsymbol{X} \; . \tag{4}$$

Using the Moore-Penrose inverse, denoted by $\dagger$, leads to

$$\boldsymbol{A} = \boldsymbol{X}'\boldsymbol{X}^{\dagger} \; . \tag{5}$$

For connections of $\boldsymbol{A}$ with the Koopman operator, see Brunton and Kutz [3]. The states are propagated through an operator $\boldsymbol{A}$ that transitions the states from snapshot to snapshot. Thus, one can write the equation for any general state, $\boldsymbol{x}_{k+1}$, as

$$\boldsymbol{x}_{k+1} \approx \boldsymbol{A}\boldsymbol{x}_k \; . \tag{6}$$

Comparing with the solution for Eq. (1) we can view the above as a discrete-time system sampled every Δt, and $\boldsymbol{A} = \exp(\mathcal{A}\Delta t)$; Kutz et al. [6]. Using Eq. (6) and noting that $\boldsymbol{A}$ can be used in an iterative fashion, with a knowledge of the initial state $\boldsymbol{x}_1$, to predict the terminal state $\boldsymbol{x}_m$ using

$$\boldsymbol{X} = \begin{bmatrix}\boldsymbol{x}_1 & \boldsymbol{A}\boldsymbol{x}_1 \cdots & \boldsymbol{A}^{m-1}\boldsymbol{x}_1\end{bmatrix} \tag{7}$$

The first step in the DMD algorithm is to compute an SVD of $\boldsymbol{X}$ as

$$\boldsymbol{X} \approx \widetilde{\boldsymbol{U}}\widetilde{\boldsymbol{\Sigma}}\widetilde{\boldsymbol{V}}^*, \tag{8}$$

$\widetilde{\boldsymbol{U}} \in \mathbb{C}^{n\times r}$, $\widetilde{\boldsymbol{\Sigma}} \in \mathbb{C}^{r\times r}$, and $\widetilde{\boldsymbol{V}} \in \mathbb{C}^{m\times r}$, and $r \leq m$ is either the exact or approximate rank of the data matrix $\boldsymbol{X}$. Here, $*$ denotes the complex conjugate transpose. Columns of $\widetilde{\boldsymbol{U}}$ are the proper orthogonal modes of $\boldsymbol{X}$ (see section 3.4 of monograph by Holmes et al. [5]) and satisfy $\widetilde{\boldsymbol{U}}\widetilde{\boldsymbol{U}}^* = \widetilde{\boldsymbol{U}}^*\widetilde{\boldsymbol{U}} = \boldsymbol{I}$. Similarly, $\widetilde{\boldsymbol{V}}\widetilde{\boldsymbol{V}}^* = \widetilde{\boldsymbol{V}}^*\widetilde{\boldsymbol{V}} = \boldsymbol{I}$. Taking the Moore-

Penrose inverse of $\boldsymbol{X}$ in Eq. (8) yields $\boldsymbol{X}^{\dagger} = \widetilde{\boldsymbol{V}}\widetilde{\boldsymbol{\Sigma}}^{-1}\widetilde{\boldsymbol{U}}^{*}$, where $^{-1}$ denotes conventional inverse, and combining with Eq. (5) yields $\boldsymbol{A}$ as

$$\boldsymbol{A} = \boldsymbol{X}'\widetilde{\boldsymbol{V}}\widetilde{\boldsymbol{\Sigma}}^{-1}\widetilde{\boldsymbol{U}}^{*}.$$

Through a similarity transformation, the expression for $\boldsymbol{A}$ is projected on to the r POD modes, Schmid [10], as

$$\widetilde{\boldsymbol{A}} = \widetilde{\boldsymbol{U}}^{*}\boldsymbol{A}\widetilde{\boldsymbol{U}} = \widetilde{\boldsymbol{U}}^{*}\boldsymbol{X}'\widetilde{V}\widetilde{\boldsymbol{\Sigma}}^{-1}\,, \tag{9}$$

which has the same non-zero eigenvectors as $\boldsymbol{A}$. We choose r by trial-and-error, and this subjectivity is a characteristic of all dimensionality reduction schemes. Matrix $\widetilde{\boldsymbol{U}}$, can be used to reconstruct he full state $\boldsymbol{x}_k$, Brunton and Kutz [3], or Chap. 13 of Smith [11] as

$$\boldsymbol{x}_k = \widetilde{\boldsymbol{U}}\widetilde{\boldsymbol{x}}_{\boldsymbol{k}}. \tag{10}$$

Eigenvectors and eigenvalues of $\widetilde{\boldsymbol{A}}$ can be obtained through $\widetilde{\boldsymbol{A}}\boldsymbol{W} = \boldsymbol{W}\boldsymbol{\Lambda}$, where $\boldsymbol{\Lambda}$ and $\boldsymbol{W}$ are the eigenvalues and eigenvectors of $\widetilde{\boldsymbol{A}}$, respectively. Schmid [10] proposed the *projected* DMD modes of size $n \times r$ using Eq. (10) as $\boldsymbol{\Phi} = \widetilde{\boldsymbol{U}}\boldsymbol{W}$; however, these are not guaranteed to be exact and Tu et al. [12] proposed the eigenvectors $\boldsymbol{\Phi}$ of the high-dimensional system as:

$$\boldsymbol{\Phi} = \boldsymbol{X}'\widetilde{\boldsymbol{V}}\widetilde{\boldsymbol{\Sigma}}^{-1}\boldsymbol{W}\,, \tag{11}$$

and showed that $\boldsymbol{A}\boldsymbol{\Phi} = \boldsymbol{\Phi}\boldsymbol{\Lambda}$; see also page 238 of Brunton and Kutz [3]. That is, the DMD modes are the eigenvectors of the higher-dimensional matrix corresponding to the eigenvalues in $\boldsymbol{\Lambda}$. Now define a transformation $\boldsymbol{x}_k = \boldsymbol{\Phi}\boldsymbol{b}_k$, which implies $\boldsymbol{b}_{k+1} = \boldsymbol{\Lambda}\boldsymbol{b}_k$; using the latter two expressions and the eigenvalue equation in Eq. (6) gives $\boldsymbol{x}_{k+1} = \boldsymbol{A}\boldsymbol{\Phi}\boldsymbol{b}_k = \boldsymbol{\Phi}\boldsymbol{\Lambda}\boldsymbol{b}_k = \boldsymbol{\Phi}\boldsymbol{\Lambda}^k\boldsymbol{b}_1$. In the last expression, we reference the initial state; and $\boldsymbol{b}_1 = \boldsymbol{\Phi}^{\dagger}\boldsymbol{x}_1$ and we can write the expression as

$$\boldsymbol{x}_{k+1} = \sum_{j=1}^{r} \boldsymbol{\phi}_j \lambda_j^k \boldsymbol{b}_1\,, \tag{12}$$

where ϕ_j and λ_j are the eigenvectors and eigenvalues, respectively. By analogy with the solution of Eq. (1), and taking $\omega_j = log(\lambda_j)/\Delta t$, and passing to continuous limit, we get

$$\boldsymbol{x}(t) = \sum_{j=1}^{r} \boldsymbol{\phi}_j e^{\omega_j t} b_j = \boldsymbol{\Phi}\exp(\boldsymbol{\Omega}t)\boldsymbol{b}_1\,, \tag{13}$$

see also page 240 of Brunton and Kutz [3] and in passing we note that $\widetilde{\boldsymbol{x}}_1 = \boldsymbol{W}\boldsymbol{\Lambda}\boldsymbol{b_1}$.

3. Transient Heat Conduction

We consider the application of DMD to the one-dimensional transient heat-conduction problem for which an analytical solution exits:

$$\frac{\partial u}{\partial t} = k\frac{\partial^2 u}{\partial x^2}\,,\ t > 0,\ 0 < x < L,$$

where u is temperature, t time, x space, and k the thermal conductivity. With the boundary conditions $u(0,t) = u(L,t) = 0$ for $t > 0$; and initial condition $u(x,0) = 100$ for $0 < x < L$. Taking $k = 0.01$, $L = 1$, obtains a solution of $u(x,t) = \sum_{n=0}^{\infty} B_n \sin\frac{n\pi x}{L} exp(-k(n\pi/L)^2 t)$, where $B_n = 200(1-\cos n\pi)/n\pi$.

Assuming $\Delta t = 2/10$ s and a spatial frequency of $\Delta x = 1/100$ m, we get 10 snapshots with each containing 100 measurements. These are post-processed using the algorithm described in Section 2. Matrix $\boldsymbol{X}$ has a size of 100×9 and $\boldsymbol{X}'$ has a size of 100 $\times 9$, and it follows that $\boldsymbol{A}$ has a size of 100 $\times 100$. Using $r = 2$ and $\widetilde{\boldsymbol{A}}$ of size $r \times r$, we get an approximate reconstruction shown in Fig. 1 along with the error of the reconstruction $|u_{DMD} - u|/u$, which is of the order of 10%. There is a spatial period to the error, which is on account of the spatial modes of the decomposition. To see this we plot

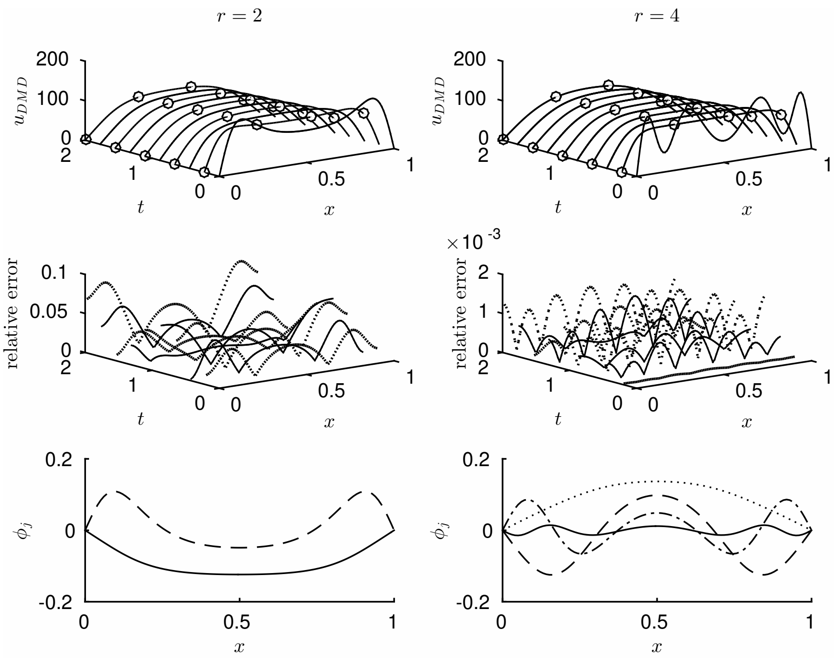

Figure 1: Left: $r = 2$, reconstructed temporal snapshots of temperature, associated error, and spatial mode shapes ϕ_j of the last snapshot . Right: $r = 4$, reconstruction, error and spatial mode shapes. Note periodicity in error owing to spatial frequency of the mode shapes.

the components of matrix $\mathbf{\Phi}$, that has a size of 100 $\times r$. Only the mode shapes of the last snapshot are shown.

When the dimension of $\widetilde{\boldsymbol{A}}$ is increased to $r = 4$, by retaining more modes, the accuracy of the surface representation improves, and the error displays more spatial periodicity as shown in the plots in Fig. 1 (right side).

4. Natural Frequency of Circular Plate

Consider vibrations of a circular plate, shown in Fig. 2, of radius 200 mm and thickness 10 mm fixed along its perimeter. A quarter-symmetry model was constructed in the Abaqus finite element solver, and meshed using linear, four-noded tetrahedra, and the Young's modulus and Poisson's ratio were taken to be 200 GPa and 0.33, respectively. A mesh size of 6 mm was used and found to guarantee convergence.

On account of needing time dependent displacements, we excited the plate with a sinusoidal velocity at its center; and the excitation frequency was taken to be 622 Hz which is close to the first natural frequency of the plate. The latter allowed us to carry out an implicit transient solution. In practice, a hammer strike will be used to excite several frequencies in the plate and drive the resonant modes, and though explicit time integration can be used to model the latter, the calculations are time consuming. The present approach serves the purpose for our demonstration.

Python scripts were used to output snapshots of nodal coordinate histories z with $\Delta t = 0.5$ ms. For linear problems with standing waves, the DMD method fails and the snapshots have to be stacked and time shifted (also called stack shifting). This increases the rank of the data matrix allowing the computation of complex conjugate eigenvectors; see

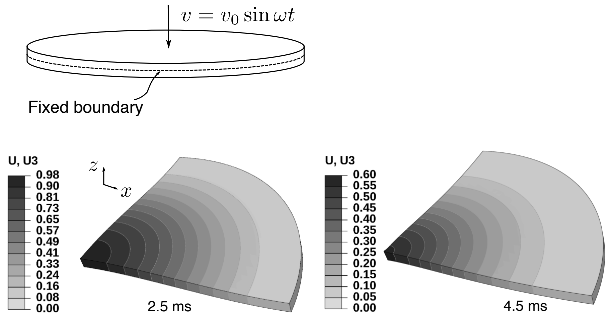

Figure 2: Circular plate clamped at the edges and loaded with a sinusoidal velocity condition. Contour plots of z displacement at two instants.

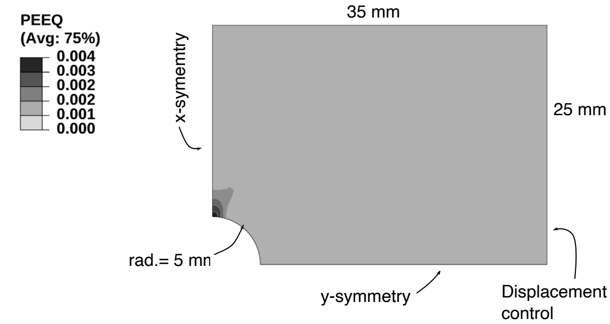

Figure 3: One-quarter of a plate with hole. Symmetry and displacement boundary conditions are shown. Contours of effective plastic strain are shown.

page 244 of Brunton and Kutz [3].

$$\boldsymbol{X} = \begin{bmatrix} \boldsymbol{x}_1, & \dots, & \boldsymbol{x_m} \\ \boldsymbol{x}_2, & \dots, & \boldsymbol{x_{m+1}} \end{bmatrix} \text{ and}$$

$$\boldsymbol{X}' = \begin{bmatrix} \boldsymbol{x}_2, & \dots, & \boldsymbol{x_{m+1}} \\ \boldsymbol{x}_3, & \dots, & \boldsymbol{x_{m+2}} \end{bmatrix}.$$

A total of 18,999 nodes were used to mesh the plate and 10 snapshots were recorded leading to a matrix $\boldsymbol{A}$, on account of the stacking, of size 75,996 $\times$75,996; in contrast, because $r = 4$, $\widetilde{\boldsymbol{A}}$ has a size of 4 $\times$4. We obtain the ωs of the $\widetilde{\boldsymbol{A}}$ as described in Section 2 and the first natural frequency of 625 Hz, which is close to the natural frequency of the system.

5. Deformation of Elastic Perfectly-Plastic Plate with hole

Consider an elastic perfectly-plate with a hole, one-quarter of which is shown in the Fig. 3, and take the Young's Modulus, Poisson's ratio, and yield strength as 200 GPa, 0.33, and 50 MPa, respectively. We use the Abaqus finite element software [1] to obtain snapshots of displacements. When the implicit solver is used to solve static problems, time is a fictitious parameter and serves as a fiducial for the loading. However, snapshots of nodal coordinates at equal intervals of time can be obtained.

The plate was meshed with linear, constant strain, plane stress triangles with a fine mesh around the perimeter of the hole. Appropriate symmetry boundary conditions were imposed and the plate was subjected to displacement controlled loading along the x-direction and the computation was carried up to the point of plastic collapse. The plate was meshed with 423 nodes, and 20 snapshots were acquired leading to an $\boldsymbol{A}$ matrix of size 846 $\times$846. Using $r = 5$, leads to a low-dimensional $\widetilde{\boldsymbol{A}}$.

Python scripts were used to obtain a total of m snapshots, doublets (x, y) in this case. We then post-processed the data and obtained the state of the plate for snapshot m using the sequence which can be used to obtain a prediction of the state of the plate for the terminal snapshot.

$$\boldsymbol{x}_m^{DMD} = [\boldsymbol{x}_1, \widetilde{\boldsymbol{U}}\widetilde{\boldsymbol{A}}\widetilde{\boldsymbol{U}}^*\boldsymbol{x}_1, \widetilde{\boldsymbol{U}}\widetilde{\boldsymbol{A}}^2\widetilde{\boldsymbol{U}}^*\boldsymbol{x}_1, \dots \\ \widetilde{\boldsymbol{U}}\widetilde{\boldsymbol{A}}^{m-1}\widetilde{\boldsymbol{U}}^*\boldsymbol{x}_1]. \tag{14}$$

Accordingly, we compute a prediction error $E_r = \sqrt{(x_p - x_t)^2 + (y_p - y_t)^2}$, which is the distance between the predicted location of the node, and the location computed using the finite element solver. The surface plot of the error is shown in Fig. 4. As can be seen the prediction error is very small throughout the plate indicating that the reduced order model has captured the displacements accu-

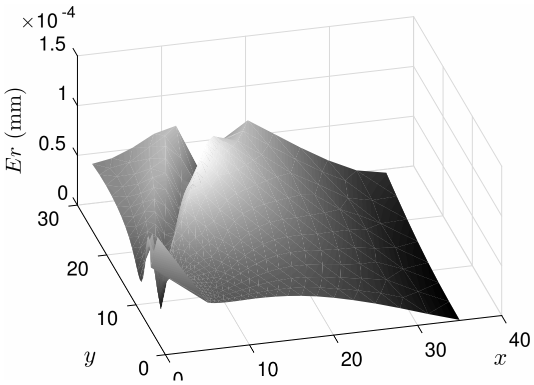

Figure 4: Surface plot of error E_r for the elastic perfectly-plastic plate with hole.

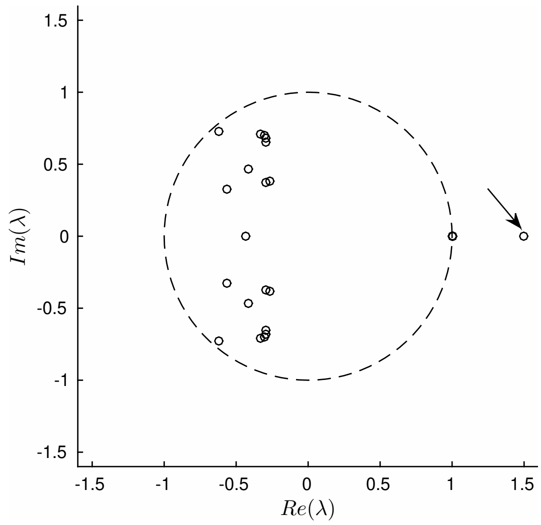

Figure 5: Plot of unit circle with eigenvalues of $\widetilde{\boldsymbol{A}}$. When it falls out of the unit circle (arrow), it is forced to a circle of radius 1.5 for clarity.

rately.

As snapshots are obtained, change in the state of the plate can also be identified using the eigenvalues of $\widetilde{\boldsymbol{A}}$. For snapshot i , we can obtain a corresponding $\widetilde{\boldsymbol{A}}$ and its eigenvalues. As each new snapshot is acquired, the eigenvalues are plotted on the complex plane as shown in Fig. 5. With the snapshot associated with the start of plasticity owing to the stress concentration, the corresponding eigenvalue lies outside the unit circle and subsequent eigenvalues will also be outside the circle. This can be interpreted as a growth mode in the physical system and that corresponds to the spreading plastic zone.

6. Reduced Order Model for Large Deformation of a Non-Linear Elastic Material

Consider a Mooney-Rivlin cantilever of length 250 mm and 25.4-mm cross section with strain energy described by

$$U = C_{10}\left(\bar{I}_1 - 3\right) + C_{01}\left(\bar{I}_2 - 3\right) + (1/D_1)\left(J^{el} - 1\right)^2,$$

where $\bar{I}_1$ and $\bar{I}_2$ are the first and second deviatoric strain invariants and J^{el} is the elastic volume, [1] We assumed C_{10} = 25 MPa, C_{01} = 0.7 MPa, D_1 = 0.00157, and a density of 1.7 kg/m^3. A total of 2129 nodes and 9328 four-noded tetrahedral elements were used to mesh the cantilever. Tip of the cantilever was displaced by (80, 80, 80) mm.

As before, implicit solver was used to carry out the simulation, and 20 snapshots of coordinates were output at equal time intervals. These were post-processed to obtain a reduced order $\widetilde{\boldsymbol{A}}$ with $r = 4$. Using Eq. (14) the deformation of the terminal snapshot was predicted and the prediction error was computed using $E_r = \sqrt{(x_p - x_t)^2 + (y_p - y_t)^2 + (z_p - z_t)^2}$. Figure 6 plots the cantilever in its original and deformed configuration, and the error contours are also shown.

It bears emphasis that the size of the $\boldsymbol{A}$ was 6387 × 6387, but we are able to describe the system with $\widetilde{\boldsymbol{A}}$ of size 8 ×8 and $\widetilde{\boldsymbol{U}}$ of size 6387 ×8. To emphasize the impact of including fewer modes, Fig. 7 displays the deformed configuration of the cantilever when r =2 and r = 8. It is apparent, that the error is 10 times higher and the shape differs significantly.

7. Summary

With the prevalence of DIC systems, structural displacement fields are readily available and the foregoing demonstrates the potential for the use of

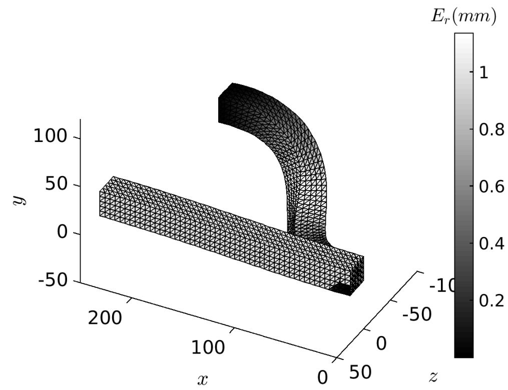

Figure 6: Square-cross section Mooney-Rivlin cantilever. Tip is displaced by (80, 80, 80) mm. Contours of E_r are shown.

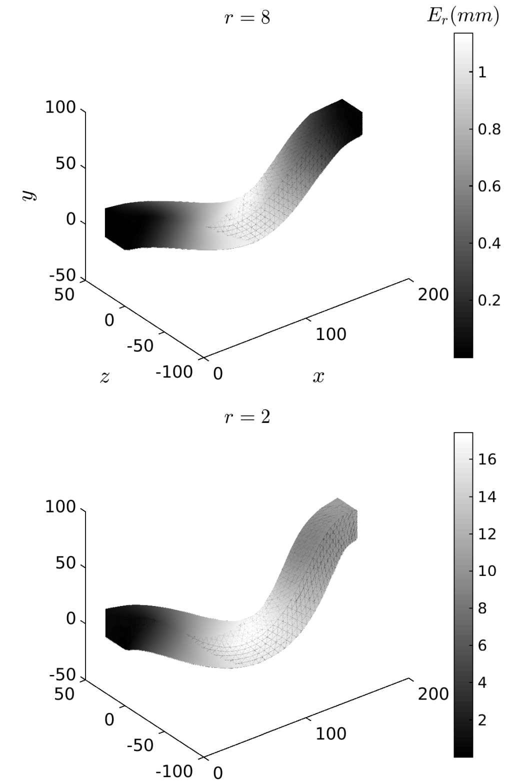

Figure 7: Effect of the number of modes r on the quality of deformation described by $\widetilde{\boldsymbol{A}}$. Contours of E_r are shown. Note the shape difference and increase in error by a factor of 10.

DMD in structural health monitoring and surrogate models for non-linear structures.

8. Acknowledgments

Funding from the Natural Sciences and Engineering Research Council of Canada through the Discovery Grant is gratefully acknowledged.

References

[1] Abaqus 6.20, 2020.

[2] W Brogan. Modern Control Theory Prentice-Hall. *Inc., New Jersey*, Second Edition, 1985.

[3] Steven L Brunton and J Nathan Kutz. *Data-driven science and engineering: Machine learning, dynamical systems, and control*. Cambridge University Press, 2019.

[4] Apurba Das, M. Nabi, and Francisco Chinesta. Modeling soft robotic actuators using data-driven model reduction. In *2020 28th Mediterranean Conference on Control and Automation (MED)*, pages 490–495, Saint-Raphaël, France, September 2020. IEEE. ISBN 978-1-72815-742-9.

[5] Philip Holmes, John L Lumley, Gahl Berkooz, and Clarence W Rowley. *Turbulence, coherent structures, dynamical systems and symmetry*. Cambridge university press, 2012.

[6] J Nathan Kutz, Steven L Brunton, Bingni W Brunton, and Joshua L Proctor. *Dynamic mode decomposition: data-driven modeling of complex systems*. SIAM, 2016.

[7] Clarence W. Rowley, Igor Mezić, Shervin Bagheri, Philipp Schlatter, and Dan S. Henningson. Spectral analysis of nonlinear flows. *Journal of Fluid Mechanics*, 641:115–127, December 2009. ISSN 0022-1120, 1469-7645.

[8] Akira Saito and Tomohiro Kuno. Data-driven experimental modal analysis by Dynamic Mode Decomposition. *Journal of Sound and Vibration*, 481:115434, September 2020.

[9] P. J. Schmid, L. Li, M. P. Juniper, and O. Pust. Applications of the dynamic mode decomposition. *Theoretical and Computational Fluid Dynamics*, 25(1-4): 249–259, June 2011.

[10] Peter J. Schmid. Dynamic mode decomposition of numerical and experimental data. *Journal of Fluid Mechanics*, 656:5–28, August 2010.

[11] Ralph C Smith. *Uncertainty quantification: theory, implementation, and applications*, volume 12. Siam, 2013.

[12] Jonathan H. Tu, Clarence W. Rowley, Dirk M. Luchtenburg, Steven L. Brunton, and J. Nathan Kutz. On dynamic mode decomposition: Theory and applications. *Journal of Computational Dynamics*, 1(2):391–421, 2014.